Developmental Cell
Article

In Vivo Imaging of Molecular Interactions at Damaged Sarcolemma

Urmas Roostalu[1,2,*] and Uwe Strähle[1,*]
[1]Institute of Toxicology and Genetics, Karlsruhe Institute of Technology and University of Heidelberg, Hermann-von-Helmholtz-Platz 1, 76344 Eggenstein-Leopoldshafen, Germany
[2]Present address: Centre for Molecular and Cellular Biology of Inflammation, King's College London, New Hunts House, Guy's Campus, London SE1 1UL, UK
*Correspondence: urmas@roostalu.info (U.R.), uwe.straehle@kit.edu (U.S.)
DOI 10.1016/j.devcel.2011.12.008

SUMMARY

Muscle cells have a remarkable capability to repair plasma membrane lesions. Mutations in dysferlin (*dysf*) are known to elicit a progressive myopathy in humans, probably due to impaired sarcolemmal repair. We show here that loss of Dysf and annexin A6 (Anxa6) function lead to myopathy in zebrafish. By use of high-resolution imaging of myofibers in intact animals, we reveal sequential phases in sarcolemmal repair. Initially, membrane vesicles enriched in Dysf together with cytoplasmic Anxa6 form a tight patch at the lesion independently of one another. In the subsequent steps, annexin A2a (Anxa2a) followed by annexin A1a (Anxa1a) accumulate at the patch; the recruitment of these annexins depends on Dysf and Anxa6. Thus, sarcolemmal repair relies on the ordered assembly of a protein-membrane scaffold. Moreover, we provide several lines of evidence that the membrane for sarcolemmal repair is derived from a specialized plasma membrane compartment.

INTRODUCTION

Because of mechanical stress, skeletal muscle cells are particularly prone to plasma membrane lesions (McNeil and Khakee, 1992). As a consequence, myofibers possess highly efficient membrane repair, which prevents cell death and circumvents costly muscle remodeling. The resealing process is proposed to rely on the generation of a new membrane barrier from internal membrane compartments (Glover and Brown, 2007; Han and Campbell, 2007). Important insight into the sarcolemmal repair was gained by the identification of DYSF as an essential component in the injury response. Mice deficient in DYSF develop healthy muscles but exhibit progressive muscular dystrophy in postnatal life (Bansal et al., 2003). Similarly, humans with mutations in the *DYSF* gene acquire limb-girdle muscular dystrophy type 2B (LGMD2B) (Bashir et al., 1998; Liu et al., 1998), Miyoshi myopathy (Liu et al., 1998), or distal myopathy with anterior tibialis onset (Illa et al., 2001). DYSF is a large (237 kDa in humans) membrane protein, suggested to be also associated with cellular vesicles (Klinge et al., 2010; Klinge et al., 2007). DYSF accumulates at the site of membrane lesion in cultured cells and has been proposed to be required for restoring cell integrity (Bansal et al., 2003; Klinge et al., 2007).

Annexins form a large protein family, characterized by their capability to bind phospholipids in a Ca^{2+}-dependent manner. Monomeric annexins can associate into multimeric complexes. The known functions of annexins include directing Ca^{2+}-regulated exocytosis or endocytosis and stabilizing various membrane compartments (Gerke et al., 2005). ANXA1 and ANXA2 were shown to bind to Dysf (Lennon et al., 2003). It has been hypothesized that the ability of annexins to form semicrystalline matrixes on artificial membrane surfaces in vitro could facilitate plasma membrane resealing (Bouter et al., 2011).

Numerous cell types have been shown to be capable of membrane repair (Glover and Brown, 2007; Han and Campbell, 2007). The visualization of this remarkably dynamic process has thus far been carried out only in cell culture-based systems with limited kinetic data (Cai et al., 2009a; Klinge et al., 2007; McNeil et al., 2006; Reddy et al., 2001). Myofibers represent a highly specialized cell type with distinct plasma membrane compartments (T-tubules), membrane-localized as well as cytoplasmic proteins (i.e., caveolin 3 [CAV3], ANXA6), and higher expression levels of genes involved in membrane resealing (*DYSF*) (Anderson et al., 1999; Farber et al., 2003; Way and Parton, 1995). Here, we have developed a high-resolution imaging method to visualize the damage response of myofibers in zebrafish muscles in real time. We demonstrate sequential steps in plasma membrane patch formation and provide evidence for a specialized membrane compartment for sarcolemmal repair.

RESULTS

Zebrafish Models for Dysferlinopathy

In order to establish the function of Dysf in zebrafish, we used RACE-PCR to isolate the full-length coding sequence. We carried out in situ hybridization and found *dysf* to be widely expressed in zebrafish muscles (see Figure S1A available online). To generate zebrafish models for Dysf deficiency-related myopathies, we designed and tested six morpholinos against exon/intron boundaries and one against the start codon. Of these morpholinos, two led to a specific phenotype and changes in Dysf transcript (Figures 1A, 1M, and 1N; Figures S1K–S1L). Embryos injected with *i36e37* morpholino developed either

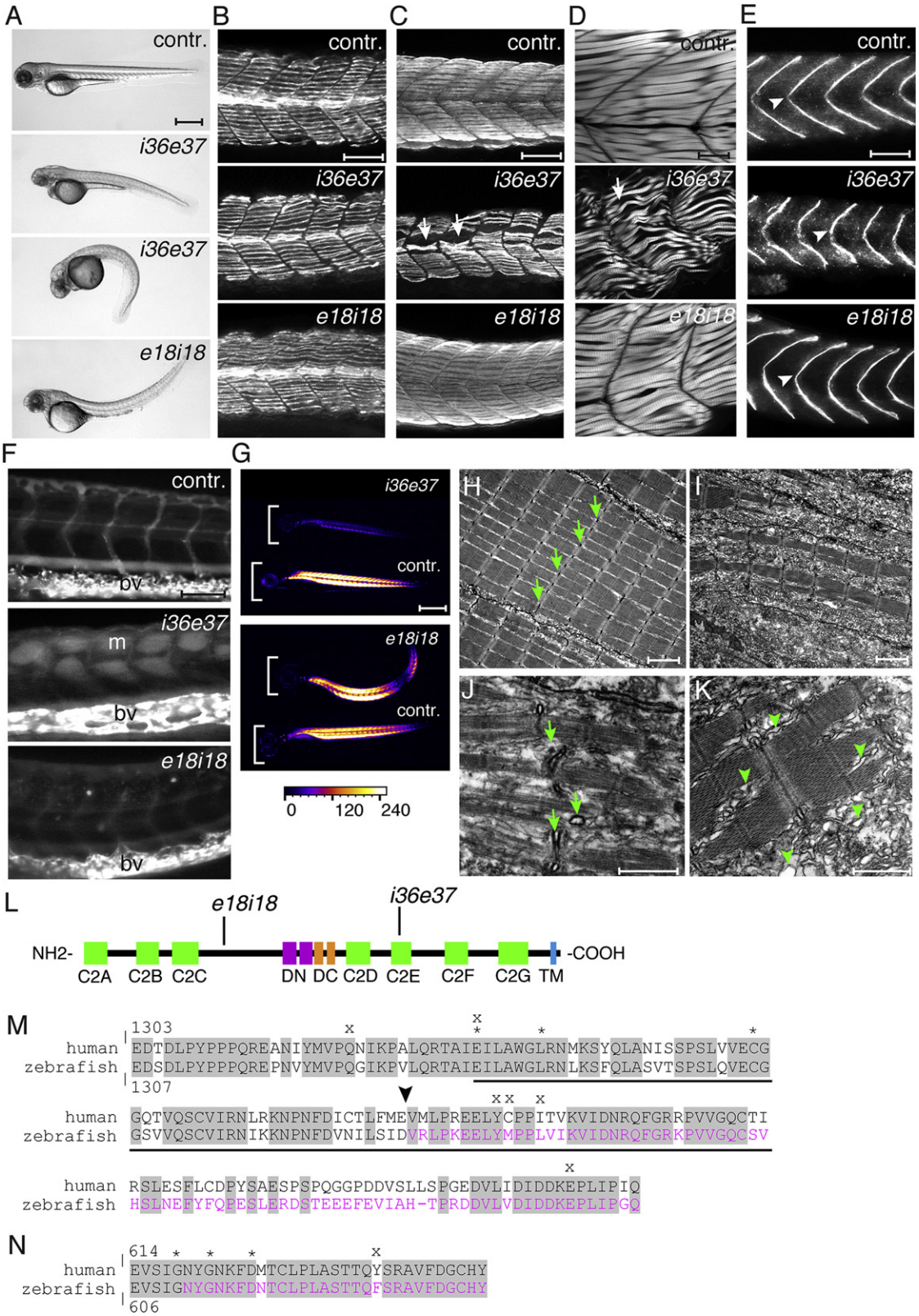

Figure 1. Zebrafish Models for Dysferlinopathy

(A) Comparison of *dysf* morpholino-injected (*i36e37*, *e18i18*) embryos with uninjected control (first panel) at 72 hpf. The *i36e37* morphants have slightly bent (second panel) or curved body (third panel), whereas *e18i18* morphants (fourth panel) have dorsally bent trunks.

a curved (7/108) or a bent (40/108) trunk at 72 hours postfertilization (hpf), and all (n = 108) acquired mild to severe cardiac edema. The blood circulation was normal, and the heartbeat was only slightly affected (Figure S1B). Slow muscle myosin staining revealed only mild defects in myofiber development at 24 hpf (n = 60) but emergence of extensive gaps in the muscle tissue by 72 hpf (all analyzed larvae, n = 60) (Figures 1B and 1C). Actin staining of deeper muscle sections confirmed the broad distribution of muscle defects (Figure 1D). Myofibers often crossed several layers, making use of cell-free spaces. The myoseptal angle in morphants (111.7° ± 1.8°) was different from that of uninjected control larvae (83.5° ± 0.8°) (Figure 1E; Figure S1C). To find out whether Dysf knockdown leads to sarcolemmal defects, we injected membrane-impermeable Evans blue dye into the pericardiac sinus at 48 hpf. Imaging at 72 hpf demonstrated accumulation of the dye in the muscle tissue in *i36e37* morphants but not in control larvae (Figure 1F). The very severe form of myopathy led to drastic and progressive loss of muscle birefringence (all analyzed larvae at 72 hpf, n = 50) (Figure 1G; Figure S1D–S1I). At the ultrastructural level, large gaps between myofibrils could be observed (Figures 1H and 1I). T-tubules were often misaligned and fragmented (Figure 1J). Accumulation of vesicles and elongated membrane compartments could be detected around myofibrils (Figure 1K).

The *e18i18* morpholino-injected larvae developed a bent trunk by 72 hpf (98/100) (Figure 1A). The myofibers were slightly misaligned (Figure 1D). However, no significant muscle damage could be observed in the larvae, and the myoseptal angle (85.3° ± 1.04°) was indistinguishable from uninjected fish (Figures 1B–1F; Figure S1C). We used mismatch control morpholinos for both *e18i18* and *i36e37* and found no change in comparison with uninjected larvae (n > 100; Figure S1J). Furthermore, a search in the zebrafish genome assembly did not reveal similar target sequences in other genes. We conclude that the phenotypes we observed are due to specific targeting of Dysf.

In silico protein domain prediction indicated that zebrafish Dysf has seven C2 domains and four Dysf domains. A putative transmembrane (TM) domain is located at the C-terminal end of the protein (Figure 1L). To characterize the morpholino-induced changes at the molecular level, RT-PCR was carried out on total RNA, extracted from single larvae. The *i36e37* morpholino leads to two different changes in *dysf* splicing (Figure S1K). First, the morphants have a transcript with the addition of intron 36, resulting in a premature stop codon and a protein, missing the three C-terminal C2 domains (C2E–C2G) and the TM domain (Figures 1L and 1M). The second transcript lacks two exons (37 and 38), causing an 80-amino acid (80-aa) deletion and removing a large part of the C2E domain (Figure 1M). Missense mutations in the C2E domain and the surrounding area have been found in patients to cause either LGMD2B or Miyoshi myopathy due to downregulation or aggregation of DYSF (Figure 1M) (De Luna et al., 2007; Guglieri et al., 2005; Kawabe et al., 2004; Krahn et al., 2009; Nguyen et al., 2005; Nguyen et al., 2007; Wenzel et al., 2006). Remarkably, the C2E domain displays a high level of evolutionary conservation (Figure 1M), supporting its importance for Dysf function. The *e18i18* morpholino leads to a 26-aa deletion in Dysf (Figure 1N; Figure S1L). The area lies outside of known protein domains but is evolutionarily very highly conserved (92.6%) between zebrafish and human (Figure 1N). Curiously, three missense substitutions have been found in this short fragment to cause myopathy (Cagliani et al., 2005; Illa et al., 2007; Krahn et al., 2009). Altogether, our data indicate that lack of Dysf leads to severe myopathy in zebrafish.

Rapid Relocation of Dysf to Membrane Lesions

We next focused on the analysis of the subcellular location of Dysf. To gain a muscle-specific expression system, we characterized the regulatory elements of the zebrafish *unc45b* gene (Figures S2A–S2D). We examined Dysf subcellular localization in myofibers by fusing monomeric teal fluorescent protein (mTFP1) to its C terminus and expressing it under the *unc45b* regulatory region. At low expression levels, Dysf-mTFP1 was distributed at the T-tubule attachment sites at the sarcolemma (Figure 2A), whereas at higher expression levels, it was detectable along the length of the sarcolemma and the T-tubules. We tested which domain of Dysf is responsible for the membrane localization by generating truncated Dysf proteins fused to mTFP1 (Figure 2B). Neither DysfN, harboring the three N-terminal C2 domains, the DysfCEN1 with the Dysf domains, nor the DysfCEN2 with the four C-terminal C2 domains resulted in accumulation of mTFP1 at membranes. In contrast, the fragment DysfC, containing the TM domain, flanked by 29 aa on the cytoplasmic side and 22 aa on the extracellular side was located at the sarcolemma (Figures 2B; Figures S2E–S2F).

(B) Embryos at 24 hpf, stained with slow muscle myosin antibody F59. No significant defects were obvious in *dysf* morphants.
(C) F59 staining at 72 hpf reveals gaps (arrow) in the muscles of *i36e37* morphants, whereas no defects were observed in *e18i18* morphants.
(D) Actin (FITC-phalloidin) staining demonstrates curved myofibers and gaps (arrow) in the *i36e37* morphant muscles. *e18i18* morphants have slightly misaligned myofibers.
(E) β-sarcoglycan staining shows differences in myoseptal (arrowhead) angle in *i36e37* morphants.
(F) Accumulation of Evans blue dye in *i36e37* morphant muscle tissue (m). bv, blood vessel.
(G) Birefringence is drastically reduced in *i36e37* morphants at 72 hpf, whereas no difference was noted in *e18i18* morphants in comparison with control larvae.
(H–K) Electron microscopy (sagittal sections) of 72 hpf myofibers. Plasma membrane is electron dense. (H) shows uninjected control larval myofiber with correctly aligned sarcomeres and T-tubules (arrows). (I) shows extensive muscle damage in *i36e37* morphant myofibers. In (J), a high-magnification image of *i36e37* morphant myofiber shows misplaced T-tubule fragments (arrows). In (K), vesicles (arrowheads) are widespread in damaged *i36e37* morphant myofibers.
(L) Zebrafish Dysf protein structure: C2, C- and N-terminal Dysf (DC and DN) as well as the TM domain are indicated. Vertical lines point to morpholino target sites.
(M) Sequence alignment of human and zebrafish Dysf C2E domain (underlined). The arrowhead points to the splice site, targeted by morpholino *i36e37*. Magenta letters outline the region, which is missing in *i36e37* morphants. Additional transcript is present in the morphants, lacking the whole protein region, downstream from the morpholino target site. Asterisks indicate mismatch substitutions that cause myopathy in humans; x denotes mutations, resulting in premature stop codon in human DYSF.
(N) Sequence alignment of the Dysf protein region targeted by *e18i18* morpholino. Letters in magenta indicate the deleted part in the morphants. Orientation of embryos A–G: anterior left, dorsal up.
Scale bars represent 500 μm (A and G); 80 μm (B, C, E, and F); 20 μm (D); 6 μm (C); 2 μm (H–I); 1 μm (J and K). See also Figure S1.

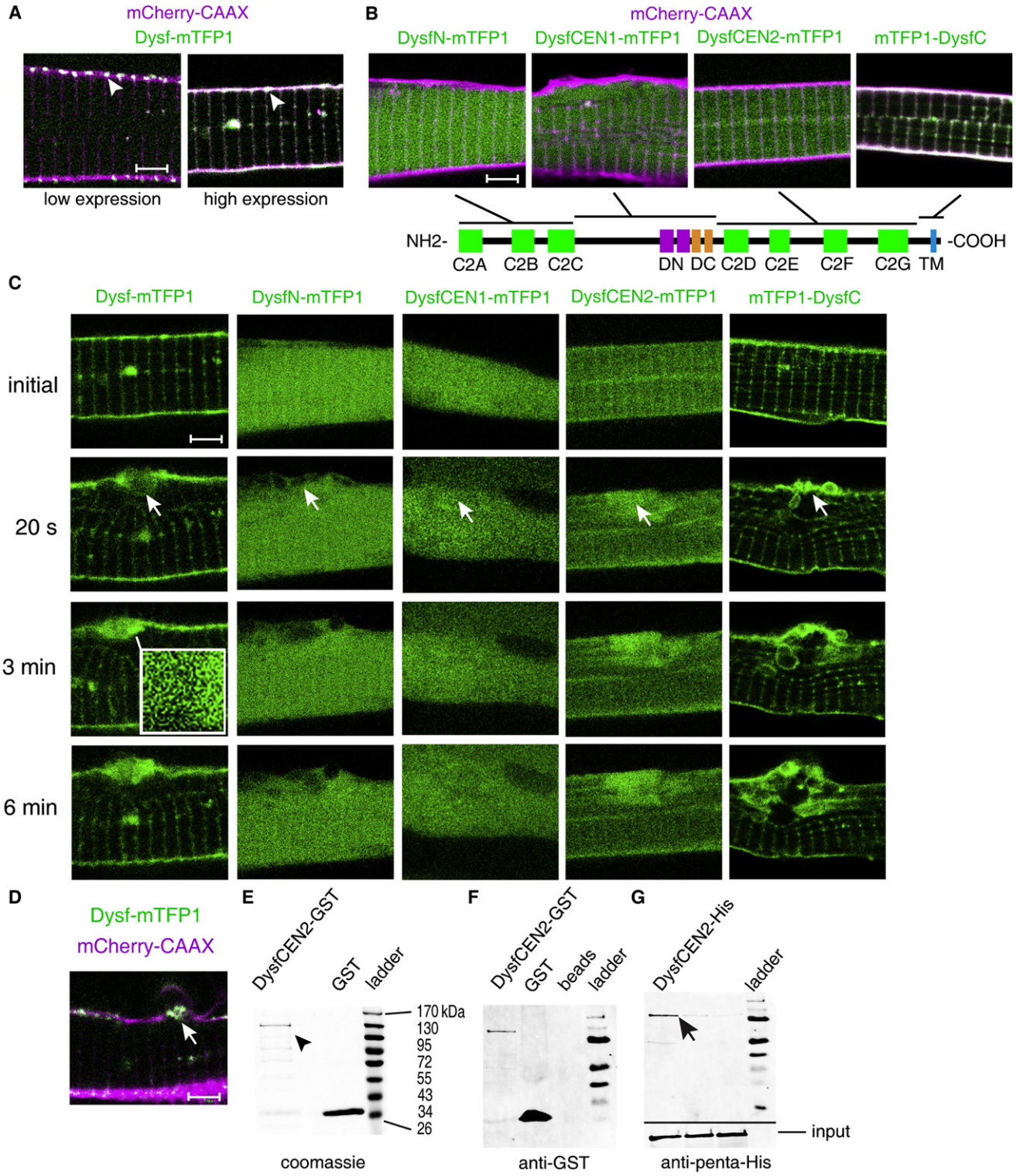

Figure 2. Characterization of Dysf and Its Response to Cell Lesions

Full-length Dysf or parts of it were fused to mTFP1 (green) and expressed in zebrafish. mCherry-CAAX marks cell membrane in magenta.

(A) At low expression levels (left), Dysf accumulates preferentially at the neck regions of T-tubules (arrowhead) but is more uniformly distributed along the plasma membrane at higher levels (right).

(B) Domain architecture of Dysf and subcellular location of individual regions. mTFP1 was fused to the C terminus, except for the TM domain (DysfC construct), where it was fused to the N-terminus. Only the C-terminal part of Dysf (DysfC) localizes to the plasma membrane.

Dysf was suggested to have a prominent role in cell membrane repair (Bansal et al., 2003), but its exact mode of function has remained elusive. By using two-photon laser pulses, we generated small sarcolemmal ruptures in 3- to 5-day-old zebrafish larvae. This enabled us to visualize protein dynamics in the intact muscle. We detected rapid Dysf-mTFP1 accumulation at the sarcolemmal lesion (Figure 2C). The accumulation did not depend on Dysf-mTFP1 expression level nor on the size of lesion (Figure 2D). Dysf appears to arrive at the site of damage on the surface of vesicular membrane structures (Figure 2C, insert). Given that Dysf-mTFP1 is primarily localized at the T-tubules and sarcolemma in undamaged myofibers, our results suggest that membrane for repair derives from the plasma membrane. Moreover, the TM and the flanking 29 N-terminal aa and 22 C-terminal aa (DysfC construct) appear to be sufficient for allocation to this compartment (Figure 2C). The C-terminal 22 aa stretch by itself does not show relocation in injured cells (Figure S2G). The N-terminal C2 domain of mammalian Dysf can interact with lipids in vitro (Therrien et al., 2009). We did not find significant membrane binding of the DysfN-mTFP1 fragment, nor did this Dysf variant accumulate in the lesion in our in vivo assay (Figure 2C). This underscores the importance of membrane insertion of Dysf in the resealing process.

We observed accumulation of the DysfCEN2 but not DysfCEN1 fragment at the lesion (Figure 2C). The four C2 domains in the C-terminal half of mammalian Dysf, corresponding to the DysfCEN2 fragment, did not show significant Ca^{2+}-dependent lipid-binding activities in vitro (Therrien et al., 2009). Because the DysfCEN2 fragment does not contain the TM domain, it is likely that it gets recruited into the repair patch in a complex with the full-length Dysf. Indeed, purified GST-tagged DysfCEN2 protein could interact with purified recombinant DysfCEN2-His (Figures 2E–2G).

Dysf Defines a Damage-Responsive Membrane Compartment

The origin of the membrane that myofibers use for sarcolemmal resealing has remained an open question. The accumulation of the sarcolemma-localized Dysf at the site of lesion indicates plasma membrane source for the repair compartment. This raises the questions of whether any part of the plasma membrane can be used for sarcolemmal repair and whether there are specific Dysf-enriched microdomains (Figures 3A and 3B). Fluorescence recovery after photobleaching (FRAP) has widely been used to study the diffusion of membrane proteins in lipid bilayers. The comparison between the recovery rates of mCherry-CAAX and mOrange1-DysfC after photobleaching of undamaged myofibers illustrates highly similar kinetics of diffusion and membrane association for the two proteins (Figure 3C). Next, the membrane markers caveolin 3 (Cav3), SNAP23 (Soluble NSF Attachment Protein 23) and mCherry-CAAX were studied in damaged myofibers. None of them showed significant accumulation in the lesion (Figures 3D and 3E; Figure S2G). In contrast, a nearly 2-fold increase of mTFP1-DysfC fluorescence (183 ± 14% at 210 s) was noted at the site of membrane rupture. The plasma membrane has specific Dysf-enriched regions that are rapidly mobilized and recruited to the damaged sarcolemma.

Studies of cell culture models predicted a role for different exocytic or endocytic vesicles in membrane repair (Idone et al., 2008; Reddy et al., 2001). We therefore analyzed whether vesicles involved in cell homeostasis could provide membrane for patch formation. We generated fusion proteins for characteristic markers of various membrane transport steps (Schwartz et al., 2007). The three zebrafish lysosome-associated membrane proteins—Laptm4a (lysosome-associated protein transmembrane 4a) and Lamp1 and Lamp2 (lysosome-associated membrane proteins 1 and 2)—did not accumulate in the lesion (Figures 3F; Figures S3A–S3D). Only when the damage was induced close to a lysosome was it incorporated in the repair patch (Figure S3D). None of the studied Rab-GTPases (Rab1a, Rab5a, Rab6a, Rab7, Rab12, and Rab27a) showed a significant increase at the sarcolemma close to the rupture, nor did they clog the lesion (Figure 3F; Figure S3E). Dysf was shown to be rapidly endocytosed through syntaxin4 (STX4) positive compartments (Evesson et al., 2010). We found no mTFP1-Stx4 accumulation at the lesion, which indicated that Stx4-mediated endocytosis is not directly involved in sarcolemmal repair (Figure 3F). In summary, our analysis of various cytoplasmic vesicle markers does not show a major involvement of cytoplasmic vesicles in providing membrane for the resealing of the sarcolemmal rupture.

Annexin Scaffold in Sarcolemmal Lesion

Annexins (A1, A2, A5, A6) have been shown to enhance plasma membrane resealing in diverse cultured cell types (Bouter et al., 2011; McNeil et al., 2006; Potez et al., 2011). *Anxa6* and *anxa11a* were shown to be expressed in zebrafish muscle (Farber et al., 2003). In addition, we detected expression of *anxa1a* and *anxa2a* transcripts in muscle (Figure S4A). RT-PCR of adult zebrafish muscle samples indicated high levels of *anxa1a, anxa2a*, and *anxa6* mRNA, whereas *anxa11a* mRNA is present at a very low level (Figure S4B). *Anxa1*, *Anxa2*, and *Anxa6* are also expressed in mammalian skeletal muscle (Bizzarro et al., 2010; Draeger et al., 2003; Lennon et al., 2003), indicating evolutionary conservation of expression.

Anxa1a, Anxa2a, Anxa6, and Anxa11a fused with mTFP1 were detectable throughout the cytoplasm in myofibers of 3- to 5-day-old larvae (Figure S4C), which is in good agreement with the cytoplasmic localization of fluorescently labeled annexins (ANXA1 and ANXA5) in cultured mammalian myoblasts and

(C) Response of Dysf, Dysf N-terminal domain (DysfN), DysfCEN1, DysfCEN2, and DysfC to membrane lesions (arrow). Dysf accumulates at the site of lesion. Vesicular structures are visible at high magnification (insert). Although DysfN and DysfCEN1 do not accumulate in the lesion, there is an increase of DysfCEN2 and DysfC.

(D) Dysf accumulation at the site of damage in a cell with a low expression level of the fusion protein.

(E) Purified DysfCEN2-GST (arrowhead) and glutathione S-transferase (GST) proteins on SDS PAGE gel.

(F and G) Protein pull-down experiment with recombinant GST- and His-tagged proteins. (F) shows an anti-GST stained western blot; (G) shows the same blot stained with anti penta-His antibody. DysfCEN2-His (97kDa, black arrow) was pulled down by DysfCEN2-GST but not with GST alone or sepharose beads. Lower section shows 20% of His-tagged protein input.

Scale bars represent 4 μm (A–D) and 0.4 μm (C insert). See also Figure S2.

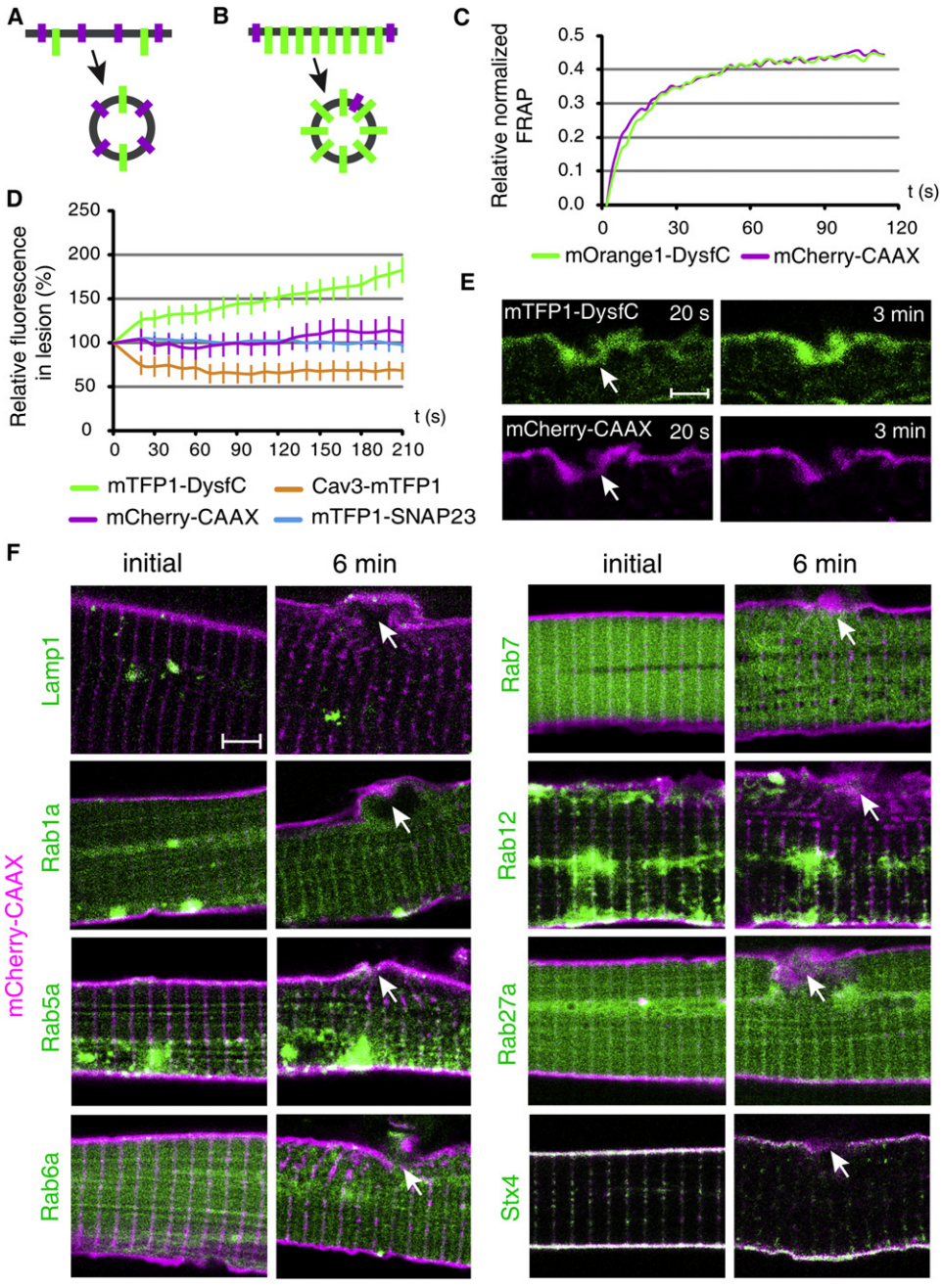

Figure 3. Origin of the Repair Membrane

(A and B) Schematic representation of the two possible sources of the sarcolemmal resealing membrane. (A) Random plasma membrane fragments, decorated with mCherry-CAAX (magenta) or Dysf (green) could provide substrate for membrane repair. (B) Specific Dysf-enriched membrane domains exist for resealing of lesions.

(C) FRAP experiment with mOrange1-tagged DysfC and mCherry-CAAX show comparable kinetics in undamaged myofibers.

(D) The TM domain of Dysf (DysfC) accumulates rapidly at the site of lesion. Much slower or no accumulation was observed for mCherry-CAAX, mTFP1-SNAP23 and Cav3-mTFP1.

(E) Coexpression of mTFP1-DysfC and mCherry-CAAX. In contrast to mTFP1-DysfC (green), mCherry-CAAX (magenta) does not accumulate in the lesion.

(F) Visualization of Lamp1-mTFP1, mTFP1-Rab1a, mTFP1-Rab5a, mTFP1-Rab6a, mTFP1-Rab7, mTFP1-Rab12, mTFP1-Rab27a, and mTFP1-Stx4 localization (green) in uninjured and injured cells. No significant relocation of the studied vesicle markers could be observed. mCherry-CAAX marks the cell membrane in magenta. White arrow indicates damaged sarcolemma.

Scale bars represent 3 μm (E) and 4 μm (F). See also Figures S2 and S3.

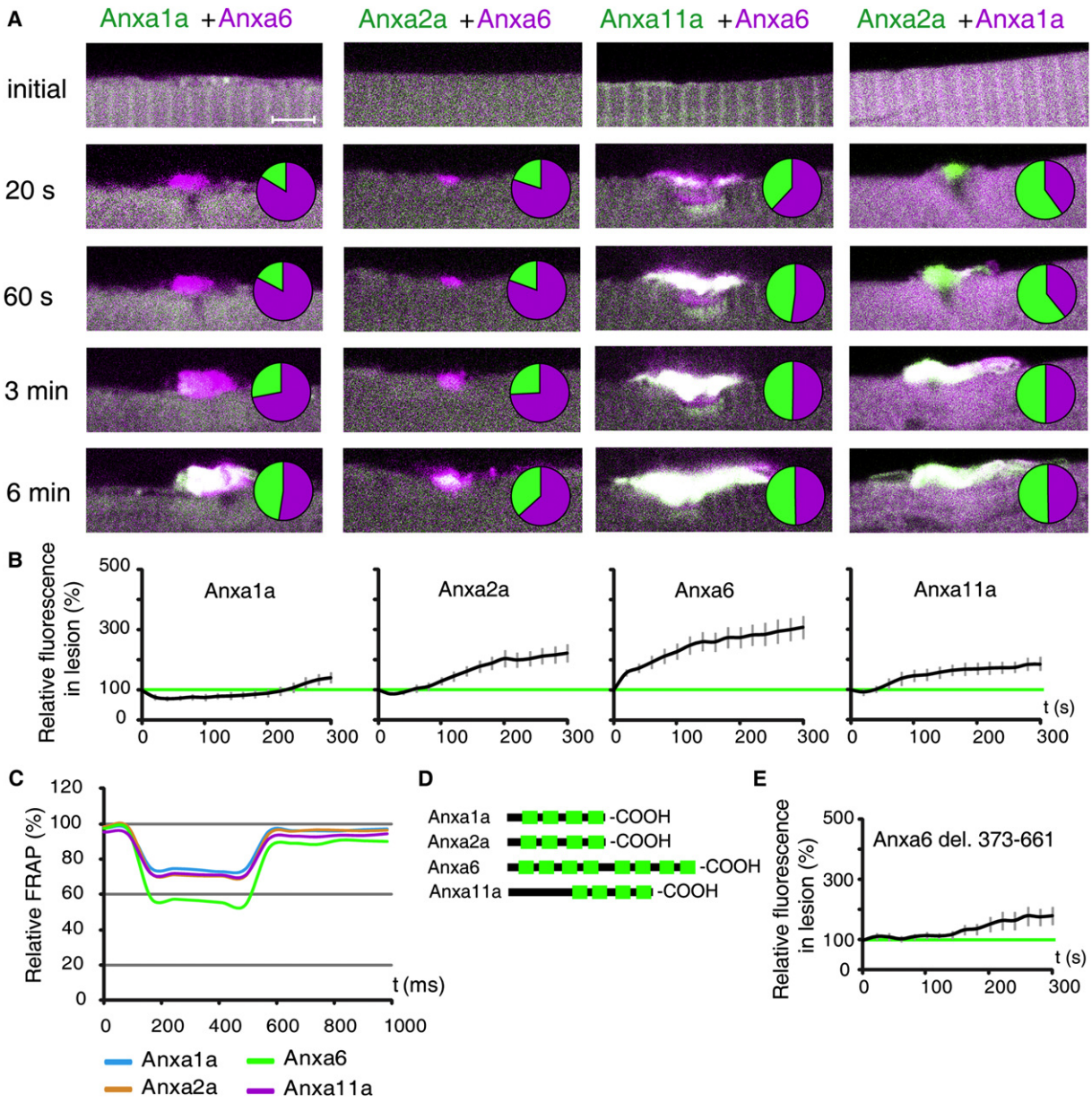

Figure 4. Annexin Kinetics in Myofibers

(A) Comparative relocation kinetics of annexins. Green letters in name or pie graph sector denote annexin tagged with mTFP1, and magenta letters indicate fusion to mOrange1. The pie graph illustrates relative intensity of the two fluorophores in the lesion. Anxa6 and Anxa11a are the fastest to accumulate in the wound, followed by Anxa2a and Anxa1a.

(B) Kinetics of mTFP1-tagged annexins at the site of the lesion (mean from eight experiments). Anxa6-mTFP1 showed a rapid increase in the lesion, whereas a time delay was observed for other annexins.

(C) FRAP was carried out with annexins tagged with mOrange1 (mean of 25 experiments). The motility of different annexins in the cytoplasm is comparable.

(D) Domain architecture of zebrafish annexins. Green boxes denote Ca^{2+}-sensitive domains. Sizes are proportional to sequence length.

(E) Accumulation of mutant Anxa6, missing the 4 C-terminal Ca^{2+}-sensing domains, is impaired in comparison with full-length Anxa6; compare with the Anxa6 panel in (B).

Scale bars represent 4 μm. See also Figure S4.

myotubes (Bizzarro et al., 2010; Cai et al., 2009a). We found that paraformaldehyde fixation induced rapid relocation of annexins to the sarcolemma (Figure S4D) similarly to membrane association of ANXA1 and ANXA2 upon immunohistochemistry on tissue sections (Lennon et al., 2003). Annexins were shown to accumulate at damaged cell membrane (Bouter et al., 2011; Cai et al., 2009a; McNeil et al., 2006; Potez et al., 2011), and we confirmed such behavior in zebrafish myofibers (Figures 4A; Figure S4E). Small wounds (less than the length of a sarcomere, < 2 μm) attracted less annexin, and the annexin patch was resolved within

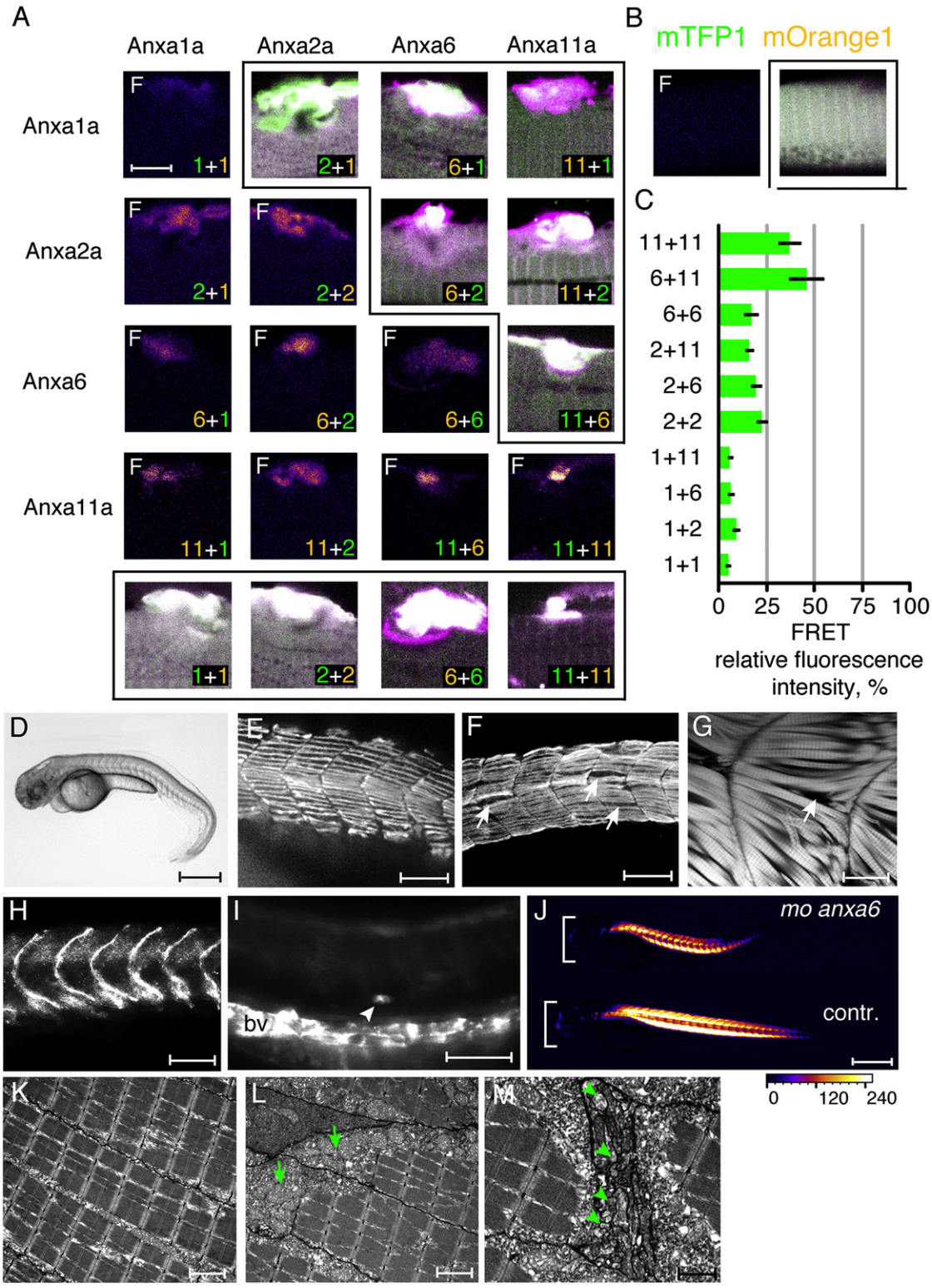

Figure 5. Distribution of Annexins in the Lesion and the *anxa6* Morphant Phenotype

(A) FRET was carried out to map the spatial distribution of annexins at high resolution. The lower triangle demonstrates FRET signal (designated as F), upper triangle and lower panel (surrounded by boxes) show the extent of damage by the colocalization of the two proteins. In each panel, the combination of annexins coexpressed are indicated by numbers (1: Anxa1a; 2: Anxa2a; 6: Anxa6; 11: Anxa11a), and the color identifies the fusion to mTFP1 (green) or mOrange1 (orange). (B) Control of FRET experiments. No FRET (left) when mOrange1 and mTFP1 were coexpressed without fusion to annexins. Overlay of mOrange and mTFP1 is shown on the right.

minutes (Figure S4F), whereas large wounds led to long-lasting annexin membrane binding (Figure S4G). We explored whether there were differences in the kinetics of accumulation of annexins at the lesion. Testing pairwise comparisons between mTFP1 and mOrange1 tagged proteins, we found that Anxa6 and Anxa11a were the fastest to accumulate at the lesion, whereas Anxa2a and Anxa1a relocated more slowly, with the latter being the slowest of the studied proteins (Figures 4A and 4B). On average, Anxa1a started to accumulate after 200–240 s, Anxa2a did so after 60–80 s, Anxa11a did so after 40 s, and no time delay could be observed for Anxa6. The differential responses did not depend on the size of the lesion or the abundance of a particular tagged annexin (Figures S4H and S4I). For example, we did not observe a significant correlation between the initial intensity of Anxa2a and its rate of accumulation by 60 s ($r = 0.28$). Anxa6 always started to accumulate by 20 s, regardless of initial expression level ($n > 50$). FRAP experiments did not reveal differences in annexin motility in undamaged myofibers (Figure 4C), which indicates that the distinct dynamics are characteristic to the proteins in injured cells. Similarly to human ANXA6 (Gerke et al., 2005), and unlike other annexins, *in silico* domain prediction supported the existence of eight Ca^{2+}-sensing domains in the zebrafish Anxa6 (Figure 4D). To confirm the requirement of these domains for a fast lesion response, we generated mutant Anxa6, lacking the four C-terminal Ca^{2+}-sensing domains. The truncated protein had significantly delayed response to sarcolemmal injury (Figure 4E), suggesting that differential sensitivity to Ca^{2+} may be one parameter that affects the speed of accumulation at the site of damage.

Experiments with purified annexins have shown that they can be aligned in a semicrystalline manner on artificial membranes (Bouter et al., 2011; Buzhynskyy et al., 2009; Illien et al., 2010; Lambert et al., 1997). We therefore tested whether such tightly packed complexes of annexins could occur at the site of lesion in vivo. We carried out fluorescence resonance energy transfer (FRET) experiments with all four annexins fused either to mOrange1 or mTFP1 to demonstrate the close placement of these proteins at the site of lesion (Figure 5A). The energy transfer distance, Förster radius (R_0), was estimated to be 5.7 nm for the mTFP1-mOrange1 fluorescent protein pair, indicative of a tight packing of the proteins (Ai et al., 2006). FRET was apparent not only between identical annexins but also between different types of annexins (Figure 5A). We did not observe FRET between annexins at sites distant to the lesion or before cell wounding (data not shown). Differences in signal intensity between different FRET pairs were evident (Figure 5C) and were in direct correlation with the arrival kinetics of annexins at the site of lesion: the more rapidly accumulating Anxa11a, Anxa6, and Anxa2a resulted in strong FRET signals.

Anxa6 Deficiency Leads to Myopathy

Because Anxa6 responds rapidly to myofiber damage, we tested its requirement in maintaining muscle integrity. We designed a morpholino, which led to a premature stop codon resulting in a truncated protein (177 aa protein in comparison with 662 aa wild-type [WT] Anxa6) (Figure S1M). Knockdown of Anxa6, similarly to the *dysf i36e37* morphants, resulted in a curved trunk in 3-day-old larvae (44/101) (Figure 5D). Early muscle development was not significantly affected ($n = 30$) (Figure 5E). However, gaps between myosin-stained slow muscle cells, as well as among actin-stained deeper myofibers, were evident at 72 hpf in all analyzed larvae ($n = 60$ for both myosin- and phalloidin-stained actin) but were more limited than in the *dysf i36e37* morphants (Figures 5F and 5G). The myoseptal angle (110.6° ± 1.2°) was significantly wider than that in uninjected control larvae (83.5° ± 0.8°) (Figure 5H; Figure S1C). On the other hand, only few cells had become permeable to Evans blue dye (Figure 5I). In contrast to the *dysf i36e37* morphants, we noted a smaller reduction in birefringence (Figure 5J). Electron microscopy demonstrated largely intact myofibers in *anxa6* morphants, with occasional cell damage (Figures 5K and 5L). Vesicles could be detected under the sarcolemma (electron dense) of ruptured myofiber (Figure 5M). Taken together, the effects of knockdown of Anxa6 are similar to but overall weaker than those of *dysf i36e37* morphants. Larvae injected with mismatch control morpholino had a WT phenotype ($n > 100$; Figure S1J).

Cumulative Role for Anxa6 and Dysf in Myofiber Maintenance

Simultaneous knockdown of Dysf (*i36e37* morpholino) and Anxa6 caused a more severe phenotype than knockdown of either of the proteins separately. All the analyzed double-morphants had a curved trunk ($n > 100$) and severe cardiac edema (Figure 6A). Muscle birefringence was almost completely absent (Figure 6B). Large cell-free spaces and severe misalignment of the myofibers could be observed (Figure 6C). The data suggest that the two proteins share functional aspects. Indeed, DysfC and the fastest annexin, Anxa6, accumulated simultaneously at the lesion (Figure 6E) with similar kinetic curves (compare Figures 3D and 4B). They also have the same spatial distribution at the lesion: the edges of the sarcolemmal lesion attracted initially both Dysf and Anxa6, from where the patch spread over the rupture (Figure 6E).

In order to analyze sarcolemmal damage induced changes at ultrastructural level, we screened for chemicals that could trigger

(C) Quantitative analysis of FRET signal intensity in the lesion (mean of five experiments).
(D) Injection of *anxa6* morpholino leads to curved trunk by 3 days of development.
(E and F) Slow muscle myosin staining (F59 antibody) shows largely normal muscle development at 24 hpf (E), but reveals gaps (arrows) between myofibers at 72 hpf (F).
(G) Deeper muscle sections were visualized with phalloidin-stained actin. Curved myofibers and gaps (arrows) were evident.
(H) β-sarcoglycan staining of obtuse myoseptal angles.
(I) Only very few cells (arrowhead) in the muscle tissue of *anxa6* morphants became penetrable to Evans blue dye. bv, blood vessel.
(J) Birefringence is only moderately affected in *anxa6* morphants.
(K–M) Electron microscopy of *anxa6* morphant myofibers. Cell membrane is electron dense. In large areas, proper myofibril organization was present (K), whereas occasional damage could also be detected (L, arrows). (M) shows accumulation of vesicles (arrowheads) at the site of myofiber damage. Orientation of embryos (D–J): anterior left, dorsal up.
Scale bars represent 6 μm (A and B); 500 μm (D and J); 80 μm (E, F, H, and I); 20 μm (G); 2 μm (K and L); 1 μm (M). See also Figure S1.

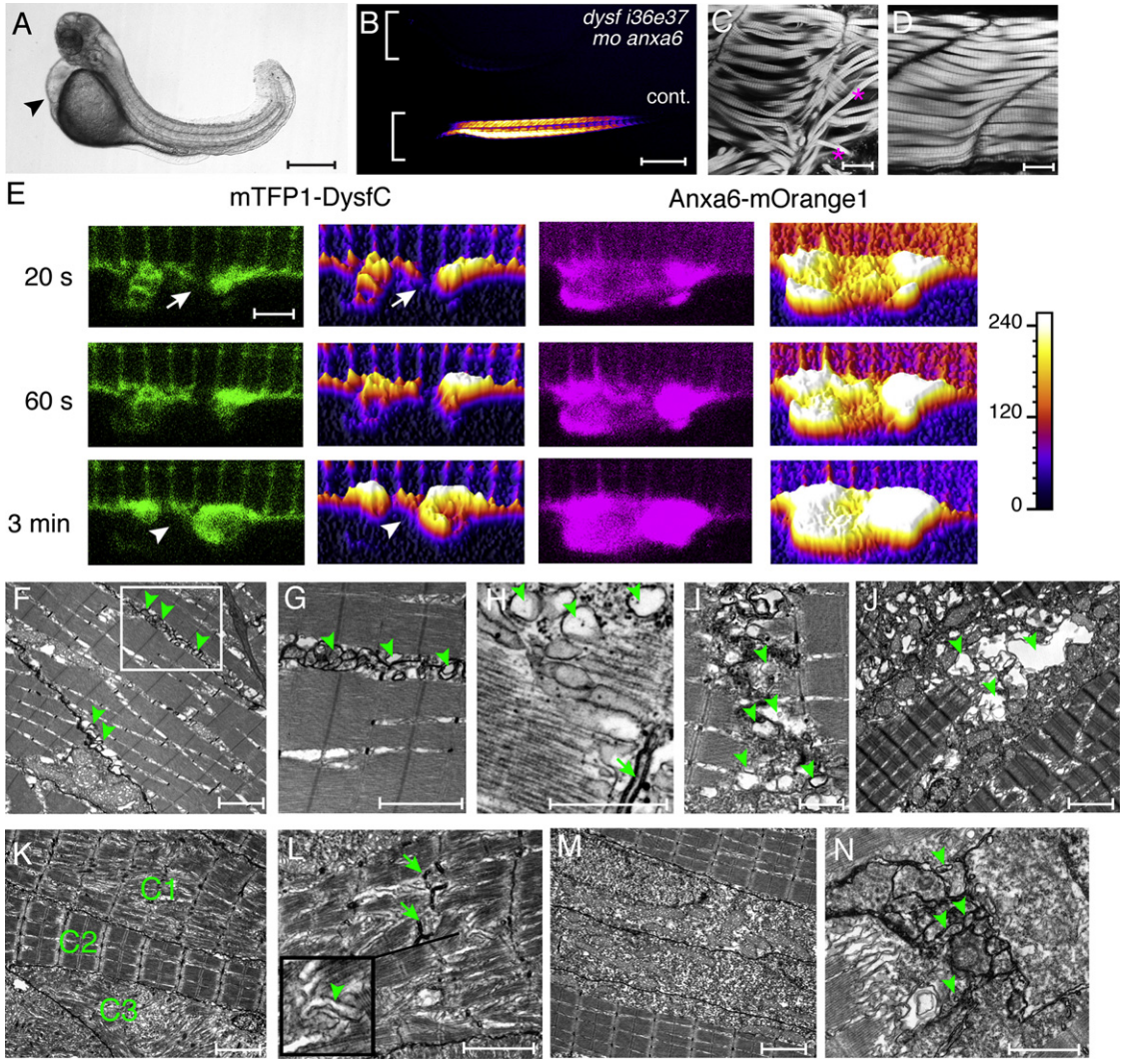

Figure 6. Anxa6/Dysf Double Morphant, Anxa6/Dysf Coexpression, and Ultrastructural Characterization of Muscle Damage

(A) Anxa6 and *dysf* (*dysf i36e37*) double morphants have curved body and severe cardiac edema (arrowhead) at 72 hpf.

(B) Muscle birefringence is almost completely absent.

(C) Misalignment (asterisks) and gaps between myofibers are visible by actin staining in the double morphants.

(D) Actin staining demonstrates normal myofiber alignment in uninjected control larvae.

(E) The accumulation of mTFP1-Dysf-coated membrane at the lesion (arrow) is rapid and coincides with Anxa6-mOrange1 appearance at the damaged sarcolemma. Increased fluorescence is depicted by lighter colors and higher surface plot profile. Note that the initial accumulation appears at the edges of the sarcolemma, from where it spreads over the damaged area, which is eventually sealed (arrowhead).

(F–N) Electron microscopy of 72 hpf myofibers. In (F), veratridine treatment leads to vesicle (arrowhead) accumulations under the sarcolemma in WT myofiber. In (G), high-magnification is shown of the boxed area in (F). In (H), cytoplasmic vesicles (arrowhead) often arise close to T-tubules (arrow). In (I), membrane blebbing and vesicles (arrowheads) could be observed at sites of fiber rupture. In (J), veratridine treatment leads to extensive muscle damage in *anxa6* morphants. Large vacuolar structures (arrowheads) can be seen around ruptured myofibers. In (K), veratridine treatment enhances muscle damage in *dysf i36e37* morphants. In some areas, correct sarcomeric filament alignment was evident (C2), whereas in other areas, it was significantly impaired (C1) or completely absent (C3).

(L) High-magnification image of veratridine-treated *dysf i36e37* morphant muscle demonstrates misaligned sarcomeres, accumulation of vesicles (arrowhead) in the cytosol and T-tubule damage (arrows). The insert shows a magnified area (1 × 1 μm).

(M and N) Anxa6 and *dysf* double morphants have severe muscle damage in untreated (M) and veratridine-treated (N) conditions. Membrane blebbing and vesicles (arrowheads) could be detected at sites of cell rupture after veratridine treatment. Orientation of embryos in (A–D): anterior left, dorsal up.

Scale bars represent 500 μm (A and B); 20 μm (C and D); 1.6 μm (E); 2 μm (F, G, and J–M); 1 μm (H, I, and N).

muscle cramps in zebrafish. Both concentric and eccentric contractility occur during cramping, which led us to hypothesize that sarcolemmal ruptures could be frequent. Veratridine leads to an increase of Na^+ and Ca^{2+} ions in muscles (Gissel and Clausen, 1999) and is a potent inducer of cramps in zebrafish. Electron microscopy of veratridine-treated larvae demonstrated mostly intact myofibers. Vesicle accumulation was occasionally observed under the sarcolemma (electron dense) (Figures 6F–6H).

Ruptured myofibers were detected, and in these areas membrane blebs and vesicles were obvious (Figure 6I). We asked whether Anxa6 or Dysf knockdown could influence muscle response to cramp-induced damage. Anxa6 morphants developed a vacuolar type myopathy in response to veratridine administration. The sarcolemmal ruptures that were observed in untreated *anxa6* morphants (Figures 5L and 5M) were significantly more prevalent on veratridine treatment (Figure 6J). Large membrane compartments were detected not only at the site of cell damage but also elsewhere between the myofibers. Dysf morphants developed also a more severe myopathy when exposed to veratridine. Myofibers demonstrated thick and thin filament misalignment. T-tubule fragmentation and extensive accumulation of vesicles were common (Figure 6K and 6L). Widespread muscle damage was evident in both untreated and veratridine-treated *anxa6* and *dysf* double morphants (Figures 6M and 6N).

Sequential Stages in Sarcolemmal Damage Response

To establish the mechanism by which Dysf and Anxa6 influence cell membrane repair, we combined morpholino experiments with quantitative intravital imaging. Knockdown of Dysf (*i36e37*), Anxa6, or both together abolished Anxa1a accumulation (Figures 7A–7C). In a similar manner, Anxa2a accumulation was significantly perturbed. Anxa2a reached predamage fluorescence intensity at the site of lesion by 40–80 s in control larvae and by 120–200 s in *dysf i36e37* morphants (Figure 7D). The accumulation of Anxa2 was even more impaired in *anxa6* morphants and almost completely absent in *dysf/anxa6* double morphants (Figures 7E and 7F). Furthermore, the morphology of the repair patch differed in the morphants. The Anxa2a patch outlined loosely packed membrane compartments (diameter up to 6 μm) that failed to generate a dense patch (Figures 7G and 7H). The large membrane blebs are similar to those observed in veratridine-treated *anxa6* morphants (Figure 6J). Knockdown of both proteins led to diffusion of Anxa2a-mTFP1 through the sarcolemmal rupture out of the cell (Figure 7I). In some myofibers (2/8), large vesicles appeared near the lesion but failed to generate a dense patch (Figure 7J). The specificity of the morpholinos was confirmed by the analysis of embryos injected with 5 base pair (bp) mismatch control morpholinos. The control morpholino did not alter repair patch formation: Anxa2a-mTFP1 accumulated within 80 s, and the resulting patch was a tightly packed structure as in WT fish (Figures S5A, S5B, S5D, and S5E). Moreover, mOrange1-tagged full-length Dysf was capable of rescuing Anxa2a-mTFP1 accumulation in the *dysf i36e37* morphants, and Anxa6-mOrange1 was sufficient to rescue the patch formation in *anxa6* morphants. Rapid accumulation of Anxa2a occurred after 80 s in rescued myofibers (Figures 7K and 7L; Figures S5F and S5G). In contrast, the short DysfC construct was incapable of rescuing the Anxa2a patch formation in *dysf i36e37* morphants, and the truncated Anxa6, lacking the 4 C-terminal Ca^{2+}-sensitive domains, was similarly inefficient in rescuing the patch formation in the *anxa6* morphants (Figure 7M; note the delayed accumulation). These experiments indicate the specificity of the rescue experiments and point to the requirement for full-length proteins in this process. In contrast to the *dysf i36e37* morphants, the patch formation occurred similarly to uninjected fish in the *dysf e18i18* morphants (Figures S5C and S5H).

Intriguingly, Dysf knockdown did not inhibit early Anxa6 recruitment to the lesion (Figure 7N), nor was the rapid accumulation of DysfC-labeled membrane perturbed in the Anxa6 morphants (Figures 7O and 7Q). Likewise, the full-length Dysf was enriched at the T-tubule attachment sites at the sarcolemma in the *anxa6* morphants and responded to membrane damage (Figure 7R). These data imply independent redistribution of the Dysf-enriched membrane and Anxa6. We detected DysfC-labeled membrane accumulation in the lesion of *dysf* morphants (Figures 7P and 7S). Although Dysf is enriched in a particular membrane domain, it does not appear to be essential for the generation of such membrane structures at the early stages of sarcolemmal repair or its transport to the lesion. Finally, on the basis of RAB27A upregulation in DYSF-deficient human myofibers, it was hypothesized that RAB27A may have a compensatory role (Kesari et al., 2008). However, mTFP1-Rab27a did not accumulate in the sarcolemmal rupture of *dysf i36e37* morphants, implying no significant contribution from this vesicle pool (Figure 7T).

DISCUSSION

We describe here zebrafish models for dysferlinopathy. Dysf knockdown does not significantly impair muscle development but, nonetheless and in contrast to the mouse model (Bansal et al., 2003), results in early myopathy. In comparison with *dysf i36e37* morphants, *anxa6* morphants show a milder phenotype. Similarly, $Dysf^{-/-}$ mice develop a more severe myopathy in contrast with the minor abnormalities in $Anxa6^{-/-}$ mice (Bansal et al., 2003; Hawkins et al., 1999; Song et al., 2002). Both mammalian DYSF and ANXA6 were shown to enhance cell recovery from membrane damage in vitro (Bansal et al., 2003; Potez et al., 2011), in agreement with our findings in zebrafish. What could explain the more severe phenotype of *dysf* morphants? There are three annexins in mature myofibers, and although we found different kinetics of accumulation, they could still cooperate with Dysf to at least partially compensate for one another. Because a cell-impermeable dye rapidly penetrated myofibers in *dysf* morphants, it is likely that Dysf-deficient muscles are more prone to membrane lesions. Extensive physical activity evoked by veratridine treatment led to even more severe defects in the *dysf* morphants, outlining the general role for Dysf in maintaining cell integrity. Such function does not appear to be limited only to sarcolemmal repair but involves a wider role in correct myofiber arrangement. In support of this, the *e18i18* morphants that lack a small fragment of Dysf have curved trunk muscles without abnormalities in repair patch formation. Similar to findings in previous data (Klinge et al., 2010), T-tubule defects were observed in Dysf knockdown myofibers, which is indicative of a role in shaping and maintaining these membrane structures. A comparable role was recently proposed for dystroglycan (Gupta et al., 2011). T-tubules are particularly vulnerable to muscle damage (Takekura et al., 2001), which is suggestive of an enhanced repair protein requirement.

A Specialized Membrane Compartment for Sarcolemmal Repair

The origin of the membrane that is used in sarcolemmal repair has remained elusive. Dysf was shown to accumulate at the site of membrane lesion in cultured myoblasts (Klinge et al.,

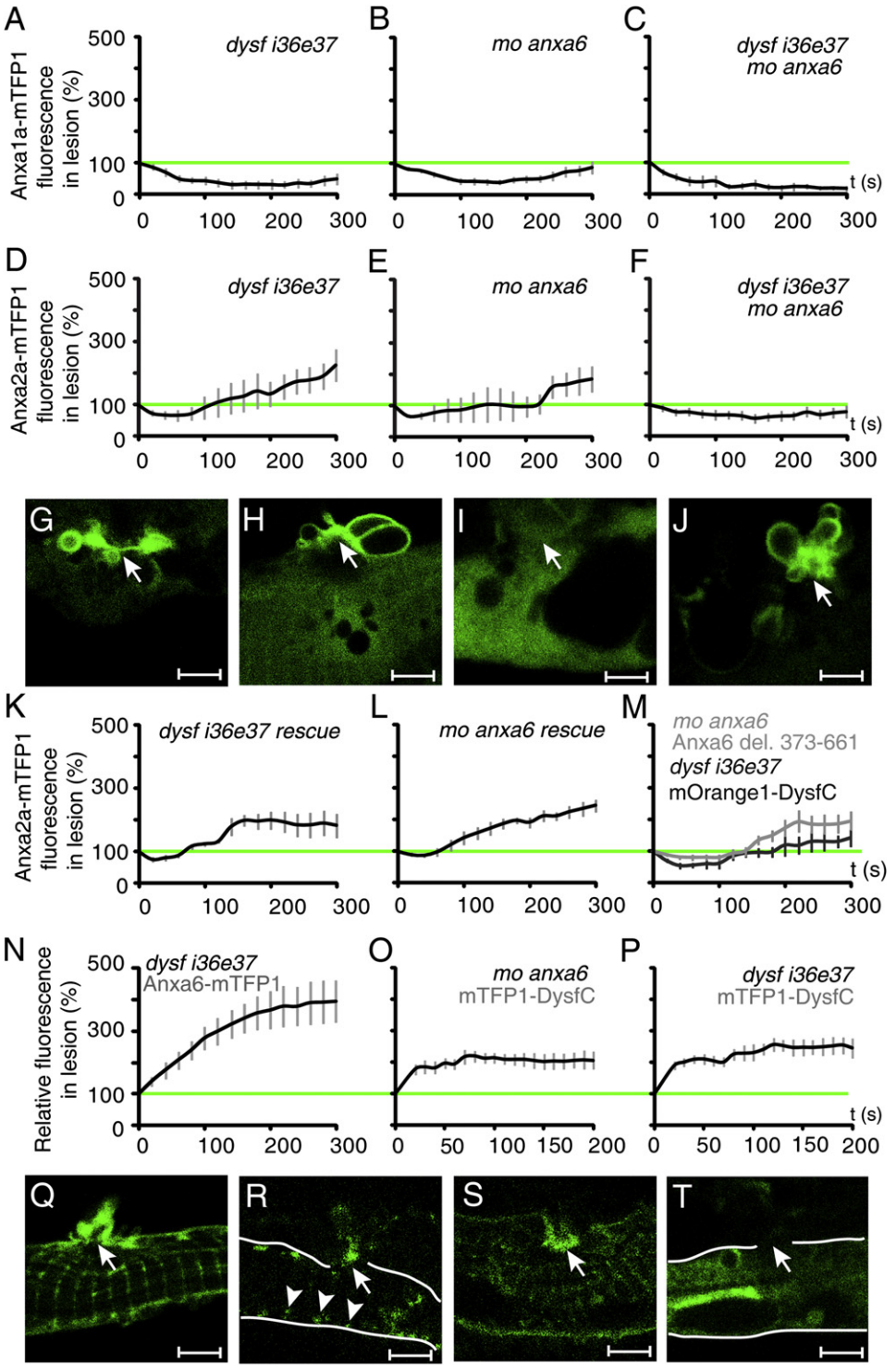

Figure 7. Functional Interactions in Repair Patch Formation

(A–I) Anxa1a accumulation is impaired in *dysf i36e37* morphants (A), *anxa6* morphants (B) and *dysf/anxa6* double morphants (C). Anxa2a-mTFP1 accumulation is delayed in *dysf i36e37* morphants (D), severely perturbed in *anxa6* morphants (E) and impaired in *dysf/anxa6* double morphants (F). The repair patch (arrow) morphology at the 3 min time point after damage (as illustrated by Anxa2a-mTFP1) is severely affected in *dysf i36e37* morphants (G) and in *anxa6* morphants (H). Anxa2a diffuses out of the cell at the 3 min time point after membrane rupture (arrow) without aggregating into a patch in double morphants (I).

(J) In a few cases, larger vesicles were visible in the double morphants.

(K) Full-length Dysf-mOrange1 rescues Anxa2a-mTFP1 recruitment in *dysf i36e37* morphants.

(L) Anxa6-mOrange1 rescues Anxa2a-mTFP1 accumulation in *anxa6* morphants.

2007). We detected prominent Dysf accumulation at the myofiber lesion on the surface of vesicles. The membrane for repair appears to arise from the plasma membrane to where Dysf is localized. As general membrane proteins (mCherry-CAAX, Cav3, SNAP23) did not show significant accumulation at the lesion, it appears that sarcolemmal resealing depends on a specialized plasma membrane compartment. The TM domain of Dysf with 29 aa at the N-terminal side and 22 aa at the C-terminal side accumulated at the lesion, suggesting that this region of Dysf is sufficient for allocation to this particular compartment. In contrast to previous cell culture studies (Idone et al., 2008; Reddy et al., 2001), we did not observe significant exocytic or endocytic vesicle recruitment at the lesion in the zebrafish myofiber.

The Role of Dysf and Annexins in Membrane Repair

Several lines of evidence suggest a late fusogenic function for Dysf. Neither the repair membrane formation nor traffic depends on Dysf. Extensive vesicle accumulation was described in ruptured *Dysf*$^{-/-}$ mouse myofibers (Bansal et al., 2003). Likewise, our electron microscopy study revealed vesicles in damaged zebrafish *dysf* morphant myofibers. Although such vesicles were hypothesized to represent a compensatory RAB27A pathway (Kesari et al., 2008), we did not detect increased Rab27a traffic toward the rupture in *dysf* knockdown myofibers. In contrast, we observed unaltered DysfC decorated membrane accumulation at the lesion in *dysf* morphants. The MG53 protein (ortholog not yet identified in zebrafish) was found to be essential for plasma membrane repair and for Dysf targeting to the lesion (Cai et al., 2009b), placing it functionally upstream of Dysf and further supporting a late role for Dysf. Finally, we found that Dysf can form homo-oligomers via the CEN2 region. It is likely that multimerization of Dysf could lead to membrane fusion at the sarcolemma in order to complete the resealing process.

The response of diverse annexins (ANXA1, ANXA2, ANXA5, ANXA6) to membrane lesions has recently gained much attention (Bouter et al., 2011; McNeil et al., 2006; Potez et al., 2011). However, the data have been restricted to cell culture systems and focused on a limited set of proteins at a time. We demonstrate here a sequential recruitment of all annexins present in the myofiber to the sarcolemmal lesion, where the proteins generate a dense patch. Considering the lipid binding capabilities of annexins (Gerke et al., 2005), they could, in addition to physically clogging the rupture, support Dysf in linking membrane structures together. In favor of such a role, we detected significantly impaired patch formation in *anxa6* morphants.

The combination of high-resolution in vivo imaging with functional data allowed us to demonstrate an unexpected complexity in the sarcolemmal patch formation. We show that, in the initial response, Dysf-enriched membrane accumulates simultaneously but independently from Anxa6. In the second phase, Anxa2a is added to the patch and finally, but several minutes later, Anxa1a covers the lesion. The accumulation of both Anxa1a and Anxa2a is impaired in *anxa6* and *dysf* morphants. It appears likely that Dysf and Anxa6 lay out the initial protein-membrane matrix, to which other proteins are subsequently added. In conclusion, we propose that the repair patch constitutes a highly ordered scaffold, where the addition of the following layer depends on the correct distribution of the previous one.

EXPERIMENTAL PROCEDURES

Detailed cloning description, list of primers, in situ hybridization, and protein purification protocols are included in the Supplemental Experimental Procedures (available online). RACE PCR (FirstChoice RLM RACE kit, Ambion) was used for obtaining full-length cDNAs of *dysf* and *anxa6* genes.

Six morpholinos against *dysf* exon/intron boundaries (the number after "e" indicates the exon number, and the number after "i" indicates the intron number: e11/i11; e18/i18; e26/i26; e31/i31; i36/e37; e43/i43) and one against the translation start site were analyzed. Only *e18/i18* (5′-GTGGTATTATCT CACCGTCGAACAC-3′) and *i36/e37* (5′-GGCAATCGCTGAAGAGAGTGCA GAA-3′) led to changed splicing. *Anxa6* morpholino (5′-TCCTGCCTCATA CAGCTCCTATAAT-3′) also induced splicing change. We used 5 bp mismatch controls (*e18/i18* contr.: 5′- GTCGAATTATGTCACCCTCCAACAC-3′; *i36/e37* contr.: 5′- GGCAAACCCTGAACAGACTCCAGAA-3′; *mo_anxa6* contr.: 5′-TCGTCCCTGATACACCTCGTATAAT-3′). All morpholinos were injected at one-cell stage at 0.8 mM concentration. For verification of splicing pattern, total RNA was extracted from 3-day-old larvae with Trizol and RT-PCR was carried out with SuperScript II reverse transcriptase. Gene-specific primers were used for the following PCR. All the PCR products were cloned to pGEM-T (Promega) and sequenced with SP6 and T7 primers.

We generated fluorescently tagged proteins by fusing them via three sequential flexible linker motifs (Gly-Gly-Gly-Gly-Ser) to the C- or N-terminus of mTFP1 or mOrange1. The choice of location of the tag was based on published data or assessed empirically. C-terminal tags were used for all annexins, Lamp1, Lamp2, Dysf, and Cav3. An N-terminal fluorescent tag was used for all Rab-GTPases, Laptm4a, Stx4, and SNAP23.

The zebrafish AB WT line was used for sarcolemmal damage experiments, and these were carried out according to approved ethical guidelines. For in vivo visualization, 3- to 5-day-old larvae were immobilized with 0.02% MESAB, immersed in a water droplet on a microscopy slide and imaged with a dip-in 63× objective (NA: 0.90; HCX APO water; Leica) and a Leica TCS SP2 confocal microscope with Leica LCS software. The observations were performed at 22°C. The sarcolemma was damaged with a two-photon laser set at 822 nm. Each protein response to membrane lesion was imaged at least 10 times. Comparative annexin kinetic properties were assessed on pairwise or

(M) Expression of mOrange1-DysfC or Anxa6 del-mOrange1 (lacking 4 C-terminal Ca^{2+}-sensitive domains) do not rescue Anxa2a-mTFP1 patch formation in *dysf i36e37* or *anxa6* morphants, respectively.
(N) Anxa6-mTFP1 rapid response is not perturbed in *dysf i36e37* morphants.
(O) mTFP1-DysfC response to membrane damage is not affected in *anxa6* morphants.
(P) Unperturbed mTFP1-DysfC accumulation at the site of sarcolemmal lesion in *dysf i36e37* morphants.
(Q) mTFP1-DysfC accumulation at the sarcolemmal rupture (arrow) in *anxa6* morphants at 60 s after damage.
(R) Full-length Dysf-mTFP1 is maintained at the T-tubule neck regions (arrowhead) and accumulates at the site of sarcolemmal lesion (arrow) in *anxa6* morphants (3 min after damage).
(S) mTFP1-DysfC accumulation at the site of sarcolemmal lesion (arrow) in *dysf i36e37* morphants at 3 min after damage.
(T) mTFP1-Rab27a does not respond to membrane damage (arrow) in *dysf i36e37* morphants (3 min after damage). In all the charts (A–F, K–P), the change at the site of lesion is indicated as percentage relative to the undamaged state (green line; mean from 6–10 experiments). Cell is outlined in white in (R) and (T). Arrow in (G–J) and (Q–T) indicates site of damage.
Scale bars represent 4 μm. See also Figure S5.

independent analysis, performed in at least five different myofibers. Kinetic curves for accumulation were based on 8–15 experiments. Error bars represent standard error of the mean in all experiments.

FRAP with mOrange1-tagged annexins was carried out in Leica fly mode: bidirectional scanning with one image per 0.082 s at 1400 Hz. A 514 nm laser was used for excitation, and emission was gathered between 550 and 650 nm. Quantification was carried out in a 19.46 μm^2 circular area. Twenty-five independent FRAP measurements were employed for each annexin, and the average kinetic parameters were calculated. For membrane proteins, the experiment was done with 800 Hz. One frame every 2 s was recorded during the recovery phase. The calculations were carried out on a rectangular sarcolemmal area (4 μm × 1.2 μm). The experiment was repeated 10 times. FRAP data were corrected for loss of fluorescence during recording and normalized to prebleach intensity. For membrane proteins, data were further normalized to equalize bleach level (Phair et al., 2004). For FRET experiments, proteins were tagged with mTFP1 and mOrange1. A 458 nm laser was used for excitation, and emission was analyzed between 610 and 700 nm. The images were normalized for differences in the expression levels of input proteins. Each annexin pair was imaged in five different cells. FRET intensity was estimated in a 6.6 μm^2 circle located at the lesion site after all the annexins had accumulated at the site of lesion (5 min). We injected 0.1% Evans blue dye in Ringer solution at 48 hpf into the pericardiac sinus and imaged at 72 hpf.

Immunohistochemistry was carried out on embryos fixed in BT-Fix solution (4% paraformaldehyde [PFA], 4% sucrose) for 1 hr at room temperature. The larvae were washed thereafter with PBS and 8 × 15 min with PBS/0.7% Triton (or PBS/0.1% Tween for the 24 hpf stage). Larvae at 72 hpf were briefly rinsed with water and incubated for 7 min at −20°C in acetone and 1 min in water. After an additional four washes in PBS/0.7% Triton or PBS/0.1% Tween, the blocking solution (1% BSA, 1% dimethyl sulfoxide [DMSO], PBS) was applied for 3 hr. Incubation with the primary antibody followed overnight at 4°C. Antibodies were anti-myosin heavy chain (F59; Developmental Studies Hybridoma Bank, The University of Iowa; Crow and Stockdale, 1986) and anti-β-sarcoglycan (Novocastra). After 8 × 15 min washes with the blocking buffer, the anti-rabbit Alexa 594 (Invitrogen) was added and incubated for 2 hr at room temperature. Actin was stained with phalloidin-FITC (Sigma-Aldrich).

In order to induce muscle cramps, we incubated 58-hpf-old zebrafish larvae overnight (until 71-72 hpf) in 30 μM veratridine (Sigma-Aldrich). Of 50 treated larvae, 5 were selected at random for electron microscopy. Larvae were fixed overnight to 2 days at 4°C in PFA and glutaraldehyde (GA) containing fixative (2% PFA; 1.25% GA; 0.1 M PIPES; 0.1% NaN_3). The larvae were washed thereafter in 0.1 M PIPES buffer (3 × 10 min), followed by second fixation (0.1M PIPES; 0.5% OsO_4; 0.8% $K_3[Fe(CN)_6]$) at 4°C on ice. The samples were washed 2 × 15 min in PIPES buffer and 2 × 15 min in water. Staining was carried out with 2% uranyl acetate (25% ethanol, 75% water) at 4°C. On the next day, the larvae were washed 2 × 15 min in PIPES buffer and dehydrated in ethanol gradient to 100% ethanol. Larvae were embedded in Epon and sectioned. A Zeiss EM109 electron microscope was used for imaging. In each fish, at least 3 myomeres were analyzed in detail, thus covering >100 myofibers.

ACCESSION NUMBERS

The NCBI database accession numbers for the sequences reported in this paper are as follows: full-length cDNA of Danio rerio dysferlin, FR725960; full-length cDNA of Danio rerio annexin A6, FR725961.

SUPPLEMENTAL INFORMATION

Supplemental Information includes five figures and Supplemental Experimental Procedures and can be found with this article online at doi:10.1016/j.devcel.2011.12.008.

ACKNOWLEDGMENTS

We thank C. Etard and M. Takamiya for kind advice and M. Rastegar for help with microscopes. We are thankful to N. Borel for help in zebrafish maintenance, T. Beil and K. Lust for assistance, and N.S. Foulkes for critical reading of the manuscript. We thank E. Schiebel and J. Roostalu for help and advice on protein biochemistry. U.R. is a recipient of a Boehringer Ingelheim PhD fellowship. We are grateful for financing from the European Commission IP ZF-Models, ZF-Health, and Association Française contre les Myopathies.

Received: February 4, 2011
Revised: October 25, 2011
Accepted: December 14, 2011
Published online: March 12, 2012

REFERENCES

Ai, H.W., Henderson, J.N., Remington, S.J., and Campbell, R.E. (2006). Directed evolution of a monomeric, bright and photostable version of Clavularia cyan fluorescent protein: structural characterization and applications in fluorescence imaging. Biochem. J. *400*, 531–540.

Anderson, L.V., Davison, K., Moss, J.A., Young, C., Cullen, M.J., Walsh, J., Johnson, M.A., Bashir, R., Britton, S., Keers, S., et al. (1999). Dysferlin is a plasma membrane protein and is expressed early in human development. Hum. Mol. Genet. *8*, 855–861.

Bansal, D., Miyake, K., Vogel, S.S., Groh, S., Chen, C.C., Williamson, R., McNeil, P.L., and Campbell, K.P. (2003). Defective membrane repair in dysferlin-deficient muscular dystrophy. Nature *423*, 168–172.

Bashir, R., Britton, S., Strachan, T., Keers, S., Vafiadaki, E., Lako, M., Richard, I., Marchand, S., Bourg, N., Argov, Z., et al. (1998). A gene related to Caenorhabditis elegans spermatogenesis factor fer-1 is mutated in limb-girdle muscular dystrophy type 2B. Nat. Genet. *20*, 37–42.

Bizzarro, V., Fontanella, B., Franceschelli, S., Pirozzi, M., Christian, H., Parente, L., and Petrella, A. (2010). Role of Annexin A1 in mouse myoblast cell differentiation. J. Cell. Physiol. *224*, 757–765.

Bouter, A., Gounou, C., Bérat, R., Tan, S., Gallois, B., Granier, T., d'Estaintot, B.L., Pöschl, E., Brachvogel, B., and Brisson, A.R. (2011). Annexin-A5 assembled into two-dimensional arrays promotes cell membrane repair. Nat Commun *2*, 270.

Buzhynskyy, N., Golczak, M., Lai-Kee-Him, J., Lambert, O., Tessier, B., Gounou, C., Bérat, R., Simon, A., Granier, T., Chevalier, J.M., et al. (2009). Annexin-A6 presents two modes of association with phospholipid membranes. A combined QCM-D, AFM and cryo-TEM study. J. Struct. Biol. *168*, 107–116.

Cagliani, R., Magri, F., Toscano, A., Merlini, L., Fortunato, F., Lamperti, C., Rodolico, C., Prelle, A., Sironi, M., Aguennouz, M., et al. (2005). Mutation finding in patients with dysferlin deficiency and role of the dysferlin interacting proteins annexin A1 and A2 in muscular dystrophies. Hum. Mutat. *26*, 283.

Cai, C., Masumiya, H., Weisleder, N., Matsuda, N., Nishi, M., Hwang, M., Ko, J.K., Lin, P., Thornton, A., Zhao, X., et al. (2009a). MG53 nucleates assembly of cell membrane repair machinery. Nat. Cell Biol. *11*, 56–64.

Cai, C., Weisleder, N., Ko, J.K., Komazaki, S., Sunada, Y., Nishi, M., Takeshima, H., and Ma, J. (2009b). Membrane repair defects in muscular dystrophy are linked to altered interaction between MG53, caveolin-3, and dysferlin. J. Biol. Chem. *284*, 15894–15902.

Crow, M.T., and Stockdale, F.E. (1986). Myosin expression and specialization among the earliest muscle fibers of the developing avian limb. Dev. Biol. *113*, 238–254.

De Luna, N., Freixas, A., Gallano, P., Caselles, L., Rojas-García, R., Paradas, C., Nogales, G., Dominguez-Perles, R., Gonzalez-Quereda, L., Vílchez, J.J., et al. (2007). Dysferlin expression in monocytes: a source of mRNA for mutation analysis. Neuromuscul. Disord. *17*, 69–76.

Draeger, A., Monastyrskaya, K., Burkhard, F.C., Wobus, A.M., Moss, S.E., and Babiychuk, E.B. (2003). Membrane segregation and downregulation of raft markers during sarcolemmal differentiation in skeletal muscle cells. Dev. Biol. *262*, 324–334.

Evesson, F.J., Peat, R.A., Lek, A., Brilot, F., Lo, H.P., Dale, R.C., Parton, R.G., North, K.N., and Cooper, S.T. (2010). Reduced plasma membrane expression of dysferlin mutants is attributed to accelerated endocytosis via a syntaxin-4-associated pathway. J. Biol. Chem. *285*, 28529–28539.

Farber, S.A., De Rose, R.A., Olson, E.S., and Halpern, M.E. (2003). The zebrafish annexin gene family. Genome Res. *13* (6A), 1082–1096.

Gerke, V., Creutz, C.E., and Moss, S.E. (2005). Annexins: linking Ca2+ signalling to membrane dynamics. Nat. Rev. Mol. Cell Biol. *6*, 449–461.

Gissel, H., and Clausen, T. (1999). Excitation-induced Ca2+ uptake in rat skeletal muscle. Am. J. Physiol. *276*, R331–R339.

Glover, L., and Brown, R.H., Jr. (2007). Dysferlin in membrane trafficking and patch repair. Traffic *8*, 785–794.

Guglieri, M., Magri, F., and Comi, G.P. (2005). Molecular etiopathogenesis of limb girdle muscular and congenital muscular dystrophies: boundaries and contiguities. Clin. Chim. Acta *361*, 54–79.

Gupta, V., Kawahara, G., Gundry, S.R., Chen, A.T., Lencer, W.I., Zhou, Y., Zon, L.I., Kunkel, L.M., and Beggs, A.H. (2011). The zebrafish dag1 mutant: a novel genetic model for dystroglycanopathies. Hum. Mol. Genet. *20*, 1712–1725.

Han, R., and Campbell, K.P. (2007). Dysferlin and muscle membrane repair. Curr. Opin. Cell Biol. *19*, 409–416.

Hawkins, T.E., Roes, J., Rees, D., Monkhouse, J., and Moss, S.E. (1999). Immunological development and cardiovascular function are normal in annexin VI null mutant mice. Mol. Cell. Biol. *19*, 8028–8032.

Idone, V., Tam, C., Goss, J.W., Toomre, D., Pypaert, M., and Andrews, N.W. (2008). Repair of injured plasma membrane by rapid Ca2+-dependent endocytosis. J. Cell Biol. *180*, 905–914.

Illa, I., Serrano-Munuera, C., Gallardo, E., Lasa, A., Rojas-García, R., Palmer, J., Gallano, P., Baiget, M., Matsuda, C., and Brown, R.H. (2001). Distal anterior compartment myopathy: a dysferlin mutation causing a new muscular dystrophy phenotype. Ann. Neurol. *49*, 130–134.

Illa, I., De Luna, N., Domínguez-Perles, R., Rojas-García, R., Paradas, C., Palmer, J., Márquez, C., Gallano, P., and Gallardo, E. (2007). Symptomatic dysferlin gene mutation carriers: characterization of two cases. Neurology *68*, 1284–1289.

Illien, F., Finet, S., Lambert, O., and Ayala-Sanmartin, J. (2010). Different molecular arrangements of the tetrameric annexin 2 modulate the size and dynamics of membrane aggregation. Biochim. Biophys. Acta *1798*, 1790–1796.

Kawabe, K., Goto, K., Nishino, I., Angelini, C., and Hayashi, Y.K. (2004). Dysferlin mutation analysis in a group of Italian patients with limb-girdle muscular dystrophy and Miyoshi myopathy. Eur. J. Neurol. *11*, 657–661.

Kesari, A., Fukuda, M., Knoblach, S., Bashir, R., Nader, G.A., Rao, D., Nagaraju, K., and Hoffman, E.P. (2008). Dysferlin deficiency shows compensatory induction of Rab27A/Slp2a that may contribute to inflammatory onset. Am. J. Pathol. *173*, 1476–1487.

Klinge, L., Laval, S., Keers, S., Haldane, F., Straub, V., Barresi, R., and Bushby, K. (2007). From T-tubule to sarcolemma: damage-induced dysferlin translocation in early myogenesis. FASEB J. *21*, 1768–1776.

Klinge, L., Harris, J., Sewry, C., Charlton, R., Anderson, L., Laval, S., Chiu, Y.H., Hornsey, M., Straub, V., Barresi, R., et al. (2010). Dysferlin associates with the developing T-tubule system in rodent and human skeletal muscle. Muscle Nerve *41*, 166–173.

Krahn, M., Béroud, C., Labelle, V., Nguyen, K., Bernard, R., Bassez, G., Figarella-Branger, D., Fernandez, C., Bouvenot, J., Richard, I., et al. (2009). Analysis of the DYSF mutational spectrum in a large cohort of patients. Hum. Mutat. *30*, E345–E375.

Lambert, O., Gerke, V., Bader, M.F., Porte, F., and Brisson, A. (1997). Structural analysis of junctions formed between lipid membranes and several annexins by cryo-electron microscopy. J. Mol. Biol. *272*, 42–55.

Lennon, N.J., Kho, A., Bacskai, B.J., Perlmutter, S.L., Hyman, B.T., and Brown, R.H., Jr. (2003). Dysferlin interacts with annexins A1 and A2 and mediates sarcolemmal wound-healing. J. Biol. Chem. *278*, 50466–50473.

Liu, J., Aoki, M., Illa, I., Wu, C., Fardeau, M., Angelini, C., Serrano, C., Urtizberea, J.A., Hentati, F., Hamida, M.B., et al. (1998). Dysferlin, a novel skeletal muscle gene, is mutated in Miyoshi myopathy and limb girdle muscular dystrophy. Nat. Genet. *20*, 31–36.

McNeil, P.L., and Khakee, R. (1992). Disruptions of muscle fiber plasma membranes. Role in exercise-induced damage. Am. J. Pathol. *140*, 1097–1109.

McNeil, A.K., Rescher, U., Gerke, V., and McNeil, P.L. (2006). Requirement for annexin A1 in plasma membrane repair. J. Biol. Chem. *281*, 35202–35207.

Nguyen, K., Bassez, G., Bernard, R., Krahn, M., Labelle, V., Figarella-Branger, D., Pouget, J., Hammouda, H., Béroud, C., Urtizberea, A., et al. (2005). Dysferlin mutations in LGMD2B, Miyoshi myopathy, and atypical dysferlinopathies. Hum. Mutat. *26*, 165.

Nguyen, K., Bassez, G., Krahn, M., Bernard, R., Laforêt, P., Labelle, V., Urtizberea, J.A., Figarella-Branger, D., Romero, N., Attarian, S., et al. (2007). Phenotypic study in 40 patients with dysferlin gene mutations: high frequency of atypical phenotypes. Arch. Neurol. *64*, 1176–1182.

Phair, R.D., Gorski, S.A., and Misteli, T. (2004). Measurement of dynamic protein binding to chromatin in vivo, using photobleaching microscopy. Methods Enzymol. *375*, 393–414.

Potez, S., Luginbühl, M., Monastyrskaya, K., Hostettler, A., Draeger, A., and Babiychuk, E.B. (2011). Tailored protection against plasmalemmal injury by annexins with different Ca2+ sensitivities. J. Biol. Chem. *286*, 17982–17991.

Reddy, A., Caler, E.V., and Andrews, N.W. (2001). Plasma membrane repair is mediated by Ca(2+)-regulated exocytosis of lysosomes. Cell *106*, 157–169.

Schwartz, S.L., Cao, C., Pylypenko, O., Rak, A., and Wandinger-Ness, A. (2007). Rab GTPases at a glance. J. Cell Sci. *120*, 3905–3910.

Song, G., Harding, S.E., Duchen, M.R., Tunwell, R., O'Gara, P., Hawkins, T.E., and Moss, S.E. (2002). Altered mechanical properties and intracellular calcium signaling in cardiomyocytes from annexin 6 null-mutant mice. FASEB J. *16*, 622–624.

Takekura, H., Fujinami, N., Nishizawa, T., Ogasawara, H., and Kasuga, N. (2001). Eccentric exercise-induced morphological changes in the membrane systems involved in excitation-contraction coupling in rat skeletal muscle. J. Physiol. *533*, 571–583.

Therrien, C., Di Fulvio, S., Pickles, S., and Sinnreich, M. (2009). Characterization of lipid binding specificities of dysferlin C2 domains reveals novel interactions with phosphoinositides. Biochemistry *48*, 2377–2384.

Way, M., and Parton, R.G. (1995). M-caveolin, a muscle-specific caveolin-related protein. FEBS Lett. *376*, 108–112.

Wenzel, K., Carl, M., Perrot, A., Zabojszcza, J., Assadi, M., Ebeling, M., Geier, C., Robinson, P.N., Kress, W., Osterziel, K.J., and Spuler, S. (2006). Novel sequence variants in dysferlin-deficient muscular dystrophy leading to mRNA decay and possible C2-domain misfolding. Hum. Mutat. *27*, 599–600.